Macro-particle simulations of collisionless magnetic reconnection

Motohiko Tanaka
National Institute for Fusion Science, Nagoya 464-01, Japan

(Received 8 July 1994; accepted 9 May 1995)

The basic process of collisionless reconnection is studied in terms of coalescence of two flux bundles using an implicit particle simulation of two-dimensions. As the toroidal electric field is generated by magnetic induction, an elongated current sheet whose width is a few electron skin depths is formed. Sub-Alfvénic plasma outflow off the reconnection region is generated in the poloidal plane which spreads within the dual fans originating at the X-point. Significant toroidal acceleration and streaming of the electrons without direct thermalization is observed in the current sheet. The electron parallel transport is proved to enhance the reconnection rate by comparing the implicit and hybrid-particle simulations; in the latter the electrons are spatially frozen to the ions. The reconnection rate is insensitive to finite Larmor radii of the ions in the regime where the magnetic flux merges constantly in time. The simulation results support that the collisionless reconnection is mediated by the electron inertia. © *1995 American Institute of Physics.*

I. INTRODUCTION

Magnetic reconnection plays a significant role in changing the topology of a magnetic field and converting magnetically stored energy to plasma bulk and thermal energies in fusion and astrophysical plasmas.[1–3] The global study of magnetic reconnection commonly relies on the MHD (magnetohydrodynamic) equations and the Ohm's law which include *ad hoc* dissipation of plasma current.[4,5] However, an origin of anomalous dissipation in high-temperature plasmas that should arise from non-Coulomb collisions has remained a key question of magnetic reconnection for many years.

For the origin of anomalous dissipation, a variety of mechanisms were proposed such as wave-particle interactions associated with microinstabilities, chaotic orbits of plasma particles, and finite inertia of the electrons. The lower-hybrid-drift instability[6,7] was once considered most promising for giving rise to anomalous resistivity in fusion and magnetospheric environments until its absence was proved at the magnetic null point due to high plasma beta. Recently, particle orbits were numerically followed to calculate the electrical conductivity for a configuration modelling the earth's magnetospheric neutral sheet.[8]

The importance of electron inertia for collisionless reconnection was first noticed in the MHD framework,[9] and then its kinetic effect was studied assuming the electromagnetic fields pertinent to magnetic reconnection.[10] Later studies focused on the collisionless process of $m=1$ tearing mode invoked by the experimental observations of fast sawtooth crash. In these studies, the MHD fluid equations and the generalized Ohm's law with electron inertia current, $E_\parallel=\eta J_\parallel+(4\pi/\omega_{pe}^2)dJ_\parallel/dt$, were adopted.[11–16] With weak dissipation $\eta J_\parallel$, the toroidal current was generated in a thin dissipation region whose spatial scale was much less than the electron skin depth; the "reconnection" electric field vanished at its center, $E_\parallel\cong dJ_\parallel/dt\to 0$, and therefore, non-zero resistivity was required to split and reconnect the magnetic field.

Nonlinear growth of a magnetic island was investigated for resistive plasmas of plain geometry[17–19] and for the collisionless $m=1$ tearing mode.[14–16] Particle simulations were performed to find energetic particles.[20,21] However, the basic issues of magnetic reconnection, especially the formation and structure of the toroidal electric field and the dissipation region, have not been well clarified because of the MHD equations or the choice of simulation parameters. Precisely, the fluid MHD simulations including the electron inertia[12,14,15] produced contradictory results depending on their adopted equations.

In fact, in the previous theories[12,15] the parallel motion of the electrons was considered only in calculating the parallel current $J_\parallel^{(e)}$, and their spatial transport due to streaming along the magnetic field was not taken into account. As will be shown in this paper (Sec. IV), the parallel transport significantly affects the collisionless reconnection rate. Moreover, if we correctly distinguish the parallel direction (the unit vector **b**) from the toroidal (y-) direction, we should have the diffusion term $(c/\omega_{pe})^2(d\ln b_y/dt)\nabla^2\Psi$ in the equation that describes the time evolution of the poloidal flux function Ψ. This term may become operative when the width of the current layer is comparable or less than the electron skin depth.

As an alternative and natural approach of elucidating the basic process of collisionless reconnection[22] without assuming the Ohm's law, we study here a coalescence process of two flux bundles by means of the $2\frac{1}{2}$-D (two space dimensions, three velocity components) electromagnetic, implicit-particle simulation method[23] (the macro-particle code "HIDEN"). The process follows the coalescence instability which is caused by magnetic attraction between the two flux bundles carrying the same-directional currents, for which the poloidal mode number is $m=2$. The coalescence is a fast process occurring in a few poloidal Alfvén times, and is observed in high-temperature, non-resistive plasmas in laboratory and astrophysical environments.[24,25] It is remarked that the coalescence process leads to magnetic reconnection without externally applying the electric field, $E_t^{(0)}=0$, and that compressibility is ignorable if the ambient magnetic field is present. These features will simplify the physical process of

 1070-664X/95/2(8)/2920/11/$6.00

collisionless reconnection and enable us to identify easily the reconnection electric field.

Concerning the methodology, the implicit particle simulation[23,26] has advantages over the conventional electromagnetic particle-in-cell simulation since it realizes large time-and-space scales while including electron dynamics, i.e., $L \gg c/\omega_{pe}$ and $\omega_{pe}\tau \gg 1$, where c is the speed of light and ω_{pe} is the electron plasma frequency. It has been proved analytically and numerically that the wave-particle resonances, complicated particle orbit effects and the electrostatic shielding due to parallel electron motions are naturally incorporated in the implicit particle simulation. Moreover, it removes intense artificial particle collisions associated with high-frequency electromagnetic and Langmuir oscillations which are inevitable in the conventional particle codes.

The present simulation algorithm[23,34] solves the complete Maxwell equations for the electromagnetic field, which are written with suffices indicating the time level,

$$\left(\frac{\partial \mathbf{E}}{\partial t}\right)^{n+1/2} = c\nabla\times\mathbf{B}^{n+\alpha} - 4\pi\mathbf{J}^{n+\alpha}, \tag{1}$$

$$\left(\frac{\partial \mathbf{B}}{\partial t}\right)^{n+1/2} = -c\nabla\times\mathbf{E}^{n+\alpha}, \tag{2}$$

$$\nabla\cdot\mathbf{E}^{n+1} = 4\pi\rho^{n+1}, \tag{3}$$

$$\nabla\cdot\mathbf{B}^{n+1} = 0, \tag{4}$$

where $\mathbf{E}$ and $\mathbf{B}$ are the electric and magnetic fields, respectively, $\mathbf{J}$ and ρ are the current and charge densities, and $\alpha > 1/2$ is the implicitness parameter. It is remarked that the Poisson equation Eq. (3) must be solved in every time step to ensure proper charge neutrality[23,34] since $\alpha \neq 1/2$ in Eq. (1). Otherwise, we would suffer from a large charge separation in the diffusion region. The Newton–Lorentz equations of motion without a collisional drag,

$$\left(\frac{d\mathbf{x}_j}{dt}\right)^{n+1/2} = \mathbf{v}_j^{n+1/2}, \tag{5}$$

$$\left(\frac{d\mathbf{v}_j}{dt}\right)^{n+1/2} = \left(\frac{e_j}{m_j}\right)\left[\mathbf{E}^{n+\alpha} + \left(\frac{\mathbf{v}_j}{c}\right)^{n+1/2}\times\mathbf{B}^{n+\alpha}\right], \tag{6}$$

are integrated in time for the new position $\mathbf{x}_j$ and velocity $\mathbf{v}_j$ of each particle, where e_j and m_j are the electric charge and mass of the jth particle. When the electrons are magnetized in the entire plasma region, we can optionally use the drift-kinetic equations for the electrons,

$$\left(\frac{d\mathbf{x}_j}{dt}\right)^{n+1/2} = [v_{\parallel j}^{n+1/2}\mathbf{b}^{n+\alpha} + \mathbf{v}_{\perp j}^{n+\alpha}], \tag{7}$$

$$\left(\frac{dv_{\parallel j}}{dt}\right)^{n+1/2} = (-e/m_e)E_{\parallel}^{n+\alpha} - \left(\frac{\mu_j}{m_e}\right)\nabla_{\parallel}B^{n+\alpha}, \tag{8}$$

where $v_{\parallel j}$, $\mathbf{v}_{\perp j}$ are the parallel and perpendicular (guiding-center) velocities, respectively, $\mathbf{b}$ is the unit vector along the magnetic field, and μ_j is the magnetic moment. To solve Eqs. (1)–(8) [or Eqs. (1)–(6)] under large time-and-space scales, the time-decentering technique is used; the choice of $\alpha > 1/2$ filters out high-frequency components of the electromagnetic oscillations for which $\omega\Delta t \gtrsim O(1)$, where ω is their characteristic frequency and Δt is a time step.

For actual solution of the electromagnetic field, Eqs. (1)–(4) are combined to obtain the pseudo-elliptic equation to determine the future electric field under a large time step. The magnetic field is then time-advanced by Eq. (2). In Eqs. (1) and (3), $\mathbf{J}$ and ρ are collected from the plasma particles by

$$\mathbf{J}(\mathbf{x}) = \sum_j e_j\mathbf{v}_j S(\mathbf{x}-\mathbf{x}_j), \qquad \rho(\mathbf{x}) = \sum_j e_j S(\mathbf{x}-\mathbf{x}_j), \tag{9}$$

where $S(\mathbf{x})$ is an assignment function satisfying $\int S(\mathbf{x})d\mathbf{x} = 1$. All the plasma particles are advanced by Eqs. (5)–(8) [or Eqs. (5), (6)] using the electromagnetic field already obtained by Eqs. (1) through (4).

In order to have a good spatial resolution of the "dissipation region" which is characterized by a peaked toroidal current J_y to be formed around $x \cong \frac{1}{2}L_x$, spatially-fixed uneven meshes are adopted in the x-direction. Furthermore, to keep the particle fluctuations in a low level, one giant particle is split into a few small particles with the (e_j/m_j) ratio fixed when it has entered the fine-mesh region located around the center of the system. On the other hand, small particles once split are not coalesced to the original size to avoid physics ambiguities.

The organization of the paper will be the following. Section II will describe the particle simulation of coalescence of two flux bundles under the ambient toroidal magnetic field. The coalescence in an unmagnetized plasma will be briefly presented in Sec. III. A hybrid-particle simulation with the same geometry and parameters as in Sec. II but forcing the electrons spatially frozen to the ions are presented in Sec. IV. This new simulation depicts an importance of parallel electron transport by streaming along the magnetic field in the collisionless reconnection. Discussions from the kinetic viewpoint, the electric field and collisionless dissipation, will also be made in Sec. IV. Finally, Sec. V will make a brief summary of the study.

II. COALESCENCE IN A MAGNETIZED PLASMA

A series of runs has been performed to study the basic process of collisionless reconnection associated with the coalescence of flux bundles. In this section, the simulation condition, parameters and results of the standard run—Run A, will be described unless otherwise specified.

A charge-neutral, homogeneous plasma is initialized with the same number of ions and electrons (64 ions/cell) in a doubly-periodic Cartesian system of the two-dimensions. The system size is $L_x = 400c/\omega_{pe}$ and $L_z = 300c/\omega_{pe}$ with 320×72 cells. The grid interval is $\Delta x \cong 0.55c/\omega_{pe}$ for the central part (107 cells) and $\Delta x \cong 1.6c/\omega_{pe}$ for the rest of the system, and $\Delta z \cong 4.1c/\omega_{pe}$ in the z-direction. Three components of the particle velocity are generated according to the Boltzmann distribution of given temperatures.

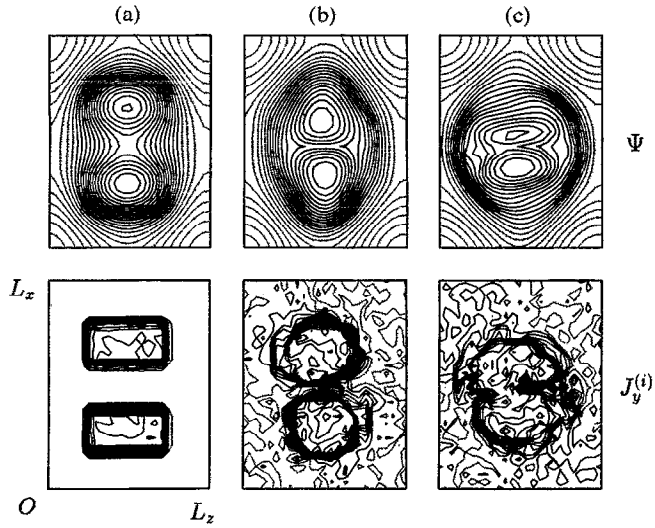

FIG. 1. Snapshots of the poloidal magnetic flux function Ψ (top), and the y-component of the ion current $J_y^{(i)}$ (bottom) for the times $t/\tau_A =$ (a) 0, (b) 1.6, and (c) 3.1. The dashed contours correspond to negative values; $\Psi_{max}=12.5$, $\Psi_{min}=-9.0$ for the upper panels, $J_t^{(i)}=0.64$ for (a), and $J_t^{(i)}=0.80$ for (b), (c) of the lower panels.

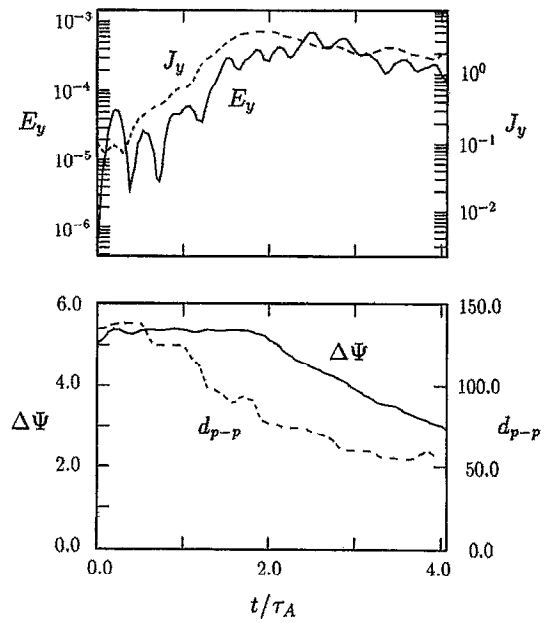

FIG. 2. Time histories of the toroidal electric field E_y (solid) and the toroidal current J_y (dashed) in the upper panel, and those of the isolated poloidal flux $\Delta\Psi$ contained in the flux bundles (solid) and the distance between the flux bundle centers d_{p-p} (dashed) in the lower panel. All of these quantities except d_{p-p} are measured in the vicinity of the X-point. The magnetic flux function is normalized as $e\Psi/m_e c^2$. (The signs of E_y and J_y are reversed.)

The ions residing in two square areas are given initial drift $V_{di}/c=0.01$ toward the positive y-direction which produces a pair of flux bundles. All the electrons drift initially at an equal velocity in the y-direction so that the plasma system has no net DC-current. (The initial flux bundle current is sustained by the ions since it makes it easier to observe the return current due to the electrons. When the initial current is assigned to the electrons, the results essentially stay the same.) The physical parameters are the mass ratio $m_i/m_e=100$, the strength of the external toroidal (y-direction) magnetic field $\omega_{ce}^{(0)}/\omega_{pe}=1$, electron beta value $\beta_e=8\pi nT_e/B^2=0.04$, and the temperature ratio $T_i/T_e=1$. The Larmor radius of thermal ions becomes $\rho_i\cong 2c/\omega_{pe}$, and the time step is $\omega_{pe}\Delta t=50$.

Figure 1 shows the poloidal magnetic flux function Ψ defined by $\mathbf{B}_p=\nabla\times(\Psi\hat{y})$, and the toroidal component of the ion current $J_y^{(i)}$ for $t/\tau_A=0$, 1.6 and 3.1. Here, the poloidal Alfvén time is defined by $\tau_A=\frac{1}{2}d/v_{Ap}\sim 3200\omega_{pe}^{-1}$, where $d=160c/\omega_{pe}$ is the initial separation of the two flux bundle centers, and $v_{Ap}=B_p^{(0)}/(4\pi m_i n)^{1/2}\sim 0.025c$ is the "poloidal" Alfvén speed. In the simulation, the flux bundles with the same-directional currents attract each other by magnetic force, and they get flatly squeezed at the contact surface as shown in Fig. 1(b) before magnetic reconnection sets in. The formation of the elongated (Y-shaped) dissipation region is the characteristic feature of the time constant flux-reconnection regime studied with MHD theories.[14,17–19] Occurrence of magnetic reconnection is roughly identified by measuring the amount of isolated poloidal magnetic flux which is contained in either of the flux bundles. The number of the isolated Ψ-contours is the same for Figs. 1(a) and 1(b), but it decreases between (b) and (c). (The total poloidal magnetic flux is conserved within three percent.)

The toroidal current of the ions shown in the lower panels of Fig. 1 gradually pinches off and its contours become more or less round-shaped in an early time because the initial plasma pressure is uniform. As the two flux bundles approach, a substantial amount of "negative" toroidal current is generated to fill in the narrow channel dividing the flux bundles (the dashed contours correspond to negative values). By this time, the channel width has been narrowed to the size comparable to electron skin depth, $L_B\cong 3c/\omega_{pe}$ (half-width). This negative current is carried mostly by the electrons, $|J_y^{(e)}/J_y^{(i)}|\sim 5$, which reaches a maximum around $t\cong 1.8\tau_A$. The intensity and area of the current sheet decrease gradually as the coalescence proceeds in the saturation stage.

The time histories of the toroidal current J_y and the electric field E_y measured in a small region at $x\cong\frac{1}{2}L_x$ are shown in Fig. 2 in logarithmic scales (the signs reversed). In the early phase up to $t\cong 2\tau_A$, the toroidal electric field E_y is observed to grow roughly exponentially with an amplitude oscillation arising from the initial loading. The sign of the E_y field at $x\cong\frac{1}{2}L_x$ stays the same during the whole simulation period, $E_y<0$. This electric field, which directly relates to magnetic reconnection through the Faraday's law Eq. (2), is purely electromagnetic (solenoidal), since a charge separation does not occur in the y-direction ($\partial\varphi/\partial y=0$ with φ the electrostatic potential). Also, the toroidal current at the X-point increases exponentially in the same growth rate as that of the E_y field. The growth phase of the toroidal electric field is succeeded at $t\cong 2\tau_A$ by a steady phase with the finite-amplitude toroidal electric field, $E_y\neq 0$ ($\partial E_y/\partial t\cong 0$). Furthermore, in the steady phase the proportionality relationship $E_y\propto J_y$ is seen at the X-point.

In the lower panel of Fig. 2, the time histories of the isolated poloidal magnetic flux and the distance between the

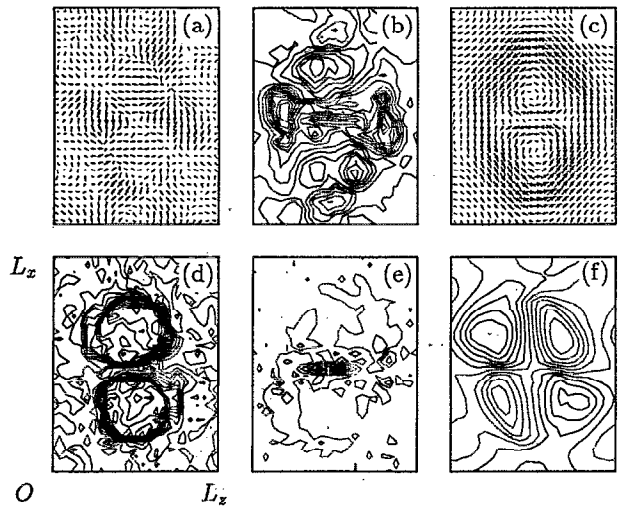

FIG. 3. (a),(b) The poloidal and toroidal electric fields, respectively; (c) the poloidal magnetic field; (d), (e) the ion and electron toroidal currents; and (f) the electrostatic potential φ at time $t=1.6\tau_A$. The maximum norms are (a) $E_p=2.1\times10^{-2}$, (b) $E_t=1.9\times10^{-3}$, (c) $B_p=0.23$, (d) $J_t^{(i)}=0.80$, (e) $J_t^{(e)}=4.0$, and (f) $\varphi=0.43$. (The electromagnetic fields are normalized as $eE/m_e c\omega_{pe}$.)

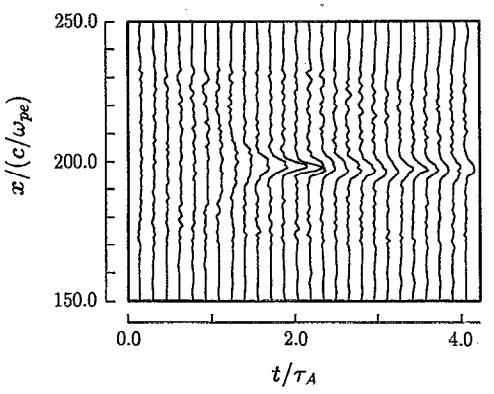

FIG. 4. The time-stacked plot of the toroidal current, $J_y(x,t)$ intersected vertically through the X-point at $z=\frac{1}{2}L_z$. The time interval between the lines is $0.16\tau_A$.

centers (peaks) of two flux bundles are shown in linear scales. The peak distance decreases with a slight bouncing motion whose period is nearly an Alfvén time. The isolated flux $\Delta\Psi$ is defined as the difference in the flux values at the peak of the flux bundle (averaged) and the separatrix. The isolated flux stays nearly the same in the early growth phase up to $t/\tau_A\cong1.8$. Then, it turns into a time-linear decrease phase which corresponds to the steady phase of the toroidal electric field. However, the flux reconnection does not continue at the same rate until $\Delta\Psi\sim0$ but slows down for $t/\tau_A\geqslant4$; approximately a third of the initially isolated flux remains unreconnected. This incomplete reconnection occurs because the two magnetic field lines contacting across the X-line become nearly parallel; this appears to be similar to the partial reconnection experiment of two co-helicity flux cores[27] (though the experiment is semi-collisional). The observed time constant annihilation of the isolated magnetic flux is consistent with nearly constant value of the toroidal electric field, as observed in Fig. 2.

Here, it is noted that, for the present mildly peaked magnetic profile, the self-driving force is rather weak and the nonlinear growth phase identified in the resistive MHD studies[17,19] is almost absent, and that the nonlinear stage with constant flux annihilation starts shortly following the onset of magnetic reconnection. The coalescence process ($m=2$) differs from the $m=1$ tearing mode[14–16] whose eigenmode structure is different.

The two-dimensional snapshots of the electric and magnetic fields, and the toroidal currents of the ions and electrons for $t/\tau_A=1.6$ are shown in Fig. 3. We note that magnetic reconnection has not started at this time. The toroidal component of the electric field E_y in panel (b) takes a positive value in the regions corresponding to the interior of the flux bundles, whereas it becomes negative in a broad region that includes the X-point. The half-width of the $E_y<0$ layer measured at $z=\frac{1}{2}L_z$ is $L_E\sim45c/\omega_{pe}$. The vertical size of the toroidal "current sheet" in Figs. 3(d) and 3(e), which characterizes the dissipation region, is much narrower than the $E_y<0$ region.

Development of the current sheet is shown in Fig. 4 with the time-stacked plot of the toroidal current which is intersected vertically through the X-point. The current sheet begins to be formed in the central region for $t>1.1\tau_A$. Its profile becomes most peaked at $t=1.8\sim2\tau_A$ just after magnetic reconnection has started. Immediately after the onset of reconnection, the width of the current sheet broadens while conserving the total amount of the current in the peak. This profile is maintained in the steady state with gradual decrease in the peak height. It is noted that, since the simulation is performed as the initial value problem, the steady state continues only for a limited period of $t\cong2\sim4\tau_A$.

Before the onset of magnetic reconnection, the toroidal electric field E_y is small on the X-line compared with the surrounding area, as seen in Fig. 3(b), because the E_y field first grows in the regions apart from the X-line. Thus, the magnetic flux first piles up on the both sides of the X-line, which was reflected on the squeezed contours of the poloidal flux function in Fig. 1(b). Meanwhile, an exponential growth of the toroidal electric field takes place as observed in Fig. 2. As the X-line turns into the global minimum of the E_y field, reconnection of the isolated magnetic flux starts.

The poloidal component of the electric field displayed in Fig. 3(a) is more intense than its toroidal component. This electric field is stationary in time and has a divergence, which is better depicted in the electrostatic potential φ of Fig. 3(f) such that $\mathbf{E}_p=-\nabla\varphi$. Obviously, the charge redistribution has occurred in a quadrupole configuration in the regions surrounding the X-point; more negative charge accumulates in the first and third quadrants with the origin at the X-point. In order to understand the origin of the poloidal electric field, the "parallel" electric field in the plasma is shown in Fig. 5(a). We define at each point the parallel electric field by $E_\parallel=E_y b_y-\mathbf{b}\cdot\nabla\varphi$, where $\mathbf{b}$ is the unit vector along the helical magnetic field. In panel (b), the projection of the static electric field onto the magnetic field, $(-\mathbf{b}\cdot\nabla\varphi)$ is

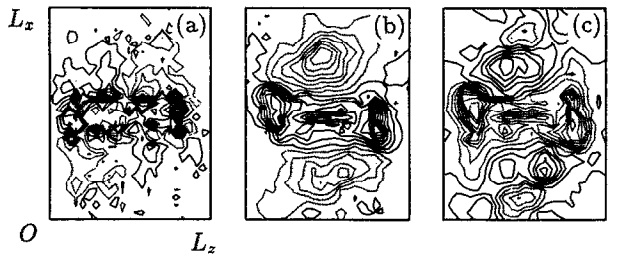

FIG. 5. (a) The parallel electric field $E_\parallel = E_y b_y - \mathbf{b}\cdot\nabla\varphi$, which is a sum of (b) projection of the poloidal electric field, $-\mathbf{b}\cdot\nabla\varphi$, and (c) that of the toroidal electric field, $E_y b_y$.

shown, and that of the inductive (solenoidal) electric field, $E_y b_y$ in panel (c). A sum of the fields of (b) and (c) is seen to be almost cancelled in (a), $E_\parallel \cong 0$, everywhere except in the vicinity of the dissipation region.

One can conclude that the electrostatic potential of the quadrupole form in Fig. 3(f) is a result of the electrostatic shielding by electron adjustment. The observation that the parallel electric field $E_\parallel$ remains unshielded is attributed to that the magnetic field is perpendicular to the x-z plane which prohibits electron charge adjustment. The electrostatic potential thus generated leads to both the E_z field laterally across the flux bundles in Fig. 3(a), and a more intense electric field E_x penetrating the dissipation region. Since the width of the layer l_x is less than its length l_z, we have $E_x/E_z \cong l_z/l_x \sim 3$. On the other hand, the net electric field $E_\parallel$ remains in the vicinity of the X-line which accelerates the light mass electrons along the magnetic field to result in the observed toroidal current sheet.

The poloidal components of the ion and electron currents, and the electric and magnetic fields in the central region are shown in Fig. 6. The magnitudes of the flow velocities are almost equal to those of the current, as the plasma is nearly uniform due to incompressibility. Both the ions and electrons stream vertically along the line connecting the flux bundle centers. The maximum inflow speed is approximately

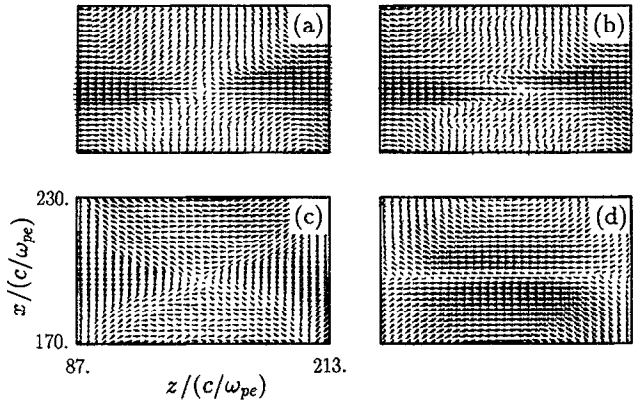

FIG. 6. Enlarged plots of poloidal quantities in the vicinity of the X-point (vectors are plotted in every four x-grid points). The ion and electron currents for the time $t = 1.6\tau_A$ in (a) and (b), respectively, and the electric and magnetic fields in (c) and (d). The maximum norms of the vectors are, (a) $J_p^{(i)} = 1.4$, (b) $J_p^{(e)} = 1.4$, (c) $E_p = 2.2\times 10^{-2}$, and (d) $B_p = 0.26$.

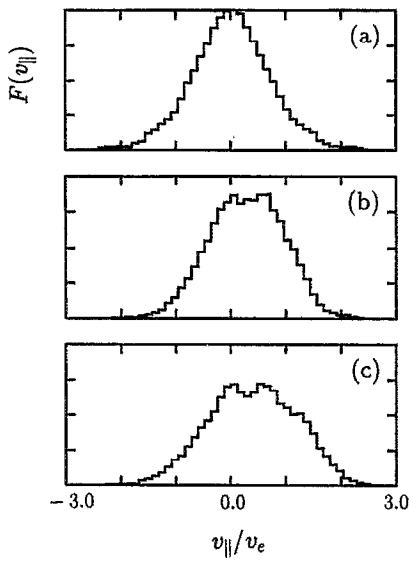

FIG. 7. The electron distribution function of the parallel velocity $F(v_\parallel)$ at the X-point. The times are (a) $t/\tau_A = 0$, (b) 1.6, and (c) 1.9, and the ordinates are in the same linear scale.

$v_{in} \sim 0.3 v_A$. The electron current in Fig. 6(b) nearly cancels that of the ions everywhere in the magnetized plasma. A slight asymmetric pattern in the electron current, i.e. antiparallel current wedges penetrating through the dissipation region, is accounted for by the ∇B drift. It is found that the flow pattern of panel (a) and the electric field of panel (c) are quite well superimposed. In addition, the observed outward velocity $v_{out} = 0.023c$ $(\sim v_{Ap})$ is faster than the inflow speed, and it coincides with $V_{E\times B} \sim 0.022c$ estimated by the poloidal electric field E_p. Thus, the plasma flow is sustained by the $E_p \times B$ drift. Here in this plasma convection, the poloidal electric field is predominant, $\mathbf{E}\times\mathbf{B} \cong \mathbf{E}_p \times \mathbf{B}_t$, and $E_x > E_z$ is consistent with $v_{out} > v_{in}$. It is stressed that the plasma outflow observed in Figs. 6(a) and 6(b) is not confined in a narrow channel defined by the poloidal magnetic field of Fig. 6(d), but that the outflow spreads within the dual fans originating at the X-point. This feature greatly differs from a square diffusion region model of Sweet and Parker.[29,30]

The electron distribution function of the parallel velocity is measured in the vicinity of the X-point. The region used for the measurement is a square of $6c/\omega_{pe} \times 30c/\omega_{pe}$ with the X-point at its center. Figure 7(b) which corresponds to just before the onset of magnetic reconnection shows a more broad profile than the initial one in (a). This may be apparently interpreted as heating, however, the velocity distribution at this time consists of two groups of the electrons whose peak velocities are either $v_\parallel \sim 0$ or $0.6 v_e$. The latter peak velocity is as large as $v_\parallel \sim 5 v_A$. The peaks in the distribution function are more clearly separated after magnetic reconnection has started in Fig. 7(c) with the peak velocities being the same as in (b). The length of the slope from the right-hand-side peak to the maximum velocity is equal to that from the left-hand-side peak to the negative maximum velocity, which reveals that the acceleration by the toroidal

electric field is responsible for the $v_\parallel > 0$ part of the distribution function. Thus, the heating we have observed in the collisionless plasma is a result of plasma acceleration and spatial mixing, and is not a direct thermalization due to magnetic reconnection.

The above observations are summarized as a natural chain to generate the toroidal electric field without resistivity. Namely, the toroidal current develops under the magnetic attraction and the electric field. This alters the poloidal magnetic field, which immediately results in the toroidal electric field by Faraday's law. The parallel electric field is not shielded but remains finite at the X-point, which accelerates the plasma to produce the toroidal current sheet. Here, we can identify three regions with (i) $J_y < 0$ (current sheet), (ii) $E_\parallel < 0$ (non-shielded region), and (iii) $E_y < 0$. The regions (i) and (ii) almost overlap, but region (iii) is much broader. These multi scale-lengths for the toroidal current and the electric field are also found for the collisionless $m=1$ mode.[15,16]

An infinite growth of the toroidal current in the dissipation region would repel the approaching flux bundles carrying the opposite-sign current and impede magnetic reconnection. Thus, its growth should stop eventually to have steady reconnection. And indeed, there is a clue which tells that the observed high-speed outflow in the poloidal plane, by which the J_y current is carried, is removing the toroidal current off the dissipation region and maintaining the steady reconnection.

In order to prove the last statement, a special run—Run B, has been designed where the poloidal electric field (E_x, E_z) is artificially reduced to 70% of its real value within the central rectangular area, $x \in \frac{1}{2}L_x \pm 10c/\omega_{pe}$, $z \in (\frac{1}{2} \pm \frac{1}{4}) \times L_z$. The other conditions are being fixed. The poloidal flux function shows that the flux bundles slide clockwise after they have encountered. The plasma density piles up in the dissipation region, and the poloidal outflow of the ions and electrons becomes quite distorted. Quantitatively, the toroidal electric field at the X-point grows exponentially in Fig. 8 but only to a lower saturation level compared to Fig. 2. Merging of the isolated flux starts but soon it slows down for $t > 2.5\tau_A$. The reconnection rate for Run B is drastically reduced from $(d\Delta\Psi/dt)/\Delta\Psi^{(0)} \sim -0.23\tau_A^{-1}$ of Run A to $-0.06\tau_A^{-1}$. Thus, it is concluded that the steady removal of the toroidal current by the poloidal plasma outflow controls the toroidal electric field at the X-point.

Here, let us look at two complementary runs to Run A that use either half the grid points in the x-direction or four times more the number of particles. These runs are performed to check the spatial resolution or particle noise effects to the simulation. In the former, the grid size at the center is $\Delta x \cong 1.1c/\omega_{pe}$, and in the latter the particle density is 256 ions (and electrons) per cell. Despite these changes, the overall results including the width of the dissipation region and the flux reconnection rate, $(d\Delta\Psi/dt)/\Delta\Psi^{(0)} \sim -0.27\tau_A^{-1}$, have stayed almost the same. If either the skin effect or numerical effects have anything to do, we should detect an appreciable difference in the structure of the current sheet and the reconnection rate. Thus, it is unlikely that the spatial resolution or the particle noise is affecting the present study of collisionless reconnection (except for resolution of a hyper-fine structure below c/ω_{pe}).

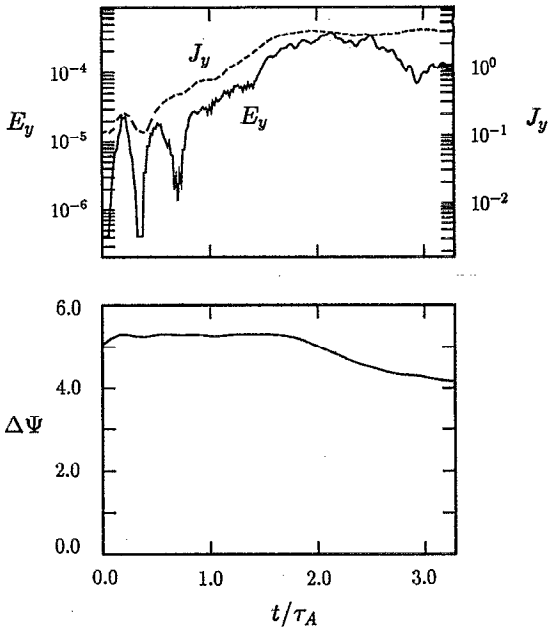

FIG. 8. Time histories of the toroidal electric field (solid), the toroidal current (dashed), and the isolated poloidal flux $\Delta\Psi$ for Run B where the poloidal electric field (E_x, E_z) in the dissipation region is reduced to 70% of its real value.

It is mentioned that the macro-particle simulation starting with the force-free equilibrium by Fadeev *et al.*[30] has reproduced the dependence of the reconnection rate on the initial magnetic profile.[31] Namely, during coalescence of the mildly peaked islands with $\epsilon = 0.3$, the magnetic flux reconnects constantly in time. By contrast, the reconnection rate is observed to increase in time and scales like $\Delta\Psi|_0^t \sim -t^2$ for the highly peaked islands with $\epsilon = 0.7$. These results are in good agreements with the MHD simulation.[32]

After having checked the simulation accuracy as stated above, the role of the ion Larmor radius effect in the coalescence process has been examined. A few other runs have been made so that the ion Larmor radius varies as $\rho_i/L_B \cong 0.4 \sim 2$, by changing either the mass ratio $m_i/m_e = 50 \sim 200$ or the ion temperature $T_i/T_e = 1 \sim 9$ (Table I). However, no appreciable change has been detected in the width of the dissipation region or the flux reconnection rate, which scatters in a range $(d\Delta\Psi/dt)/\Delta\Psi^{(0)} \sim -(0.23 \sim 0.27)\tau_A^{-1}$. Thus, it is concluded that collisionless reconnection is governed by the electron dynamics in the constant flux-reconnection regime.

III. COALESCENCE IN A NON-MAGNETIZED PLASMA

Another series of the coalescence simulation has been made using the same initial geometry and parameters, but without imposing the external magnetic field $B_t^{(0)}$. Because of the presence of the magnetic-null point in the plasma, the electron orbits are fully traced using the Newton-Lorentz equations, Eqs. (5) and (6). The maximum strength of the

TABLE I. A series of runs with different ion Larmor radii.

Mass dependence ($T_i/T_e=1$)			
$\frac{m_i}{m_e}$	50.	100.	200.
$\frac{1}{\Psi}\frac{d\Delta\Psi}{dt}$	$0.25\tau_A^{-1}$	$0.23\tau_A^{-1}$	$0.29\tau_A^{-1}$
Temperature dependence ($m_i/m_e=100$)			
T_i/T_e	1.	4.	9.
ρ_i/L_B	2./3.	4./3.	6./3.
$\frac{1}{\Psi}\frac{d\Delta\Psi}{dt}$	$0.23\tau_A^{-1}$	$0.27\tau_A^{-1}$	$0.26\tau_A^{-1}$

magnetic field for this run is $|B|\cong 0.25$ and the ion Larmor radius becomes $\rho_i \cong 8c/\omega_{pe}$. The time step is $\omega_{pe}\Delta t = 5$.

As the two flux bundles coalesce, the poloidal current into and off the dissipation region is formed. A remarkable difference in the $B_t^{(0)}=0$ case is that, in contrast to the ion outward current within the dual fan-shape which is similar to that in Fig. 6(a), the electron current tends to be rather concentrated in an unmagnetized channel along the X-line. Thus, the electron poloidal current exceeds that of the ions along the X-line. This net poloidal current is equivalent to four current vortices located in each quadrant around the X-point, which produces a quadrupole structure in the toroidal magnetic field. The toroidal electric field E_y is generated before the reconnection starts in a wide X-shaped region that covers the X-point, in a similar way as described in Sec. II. By contrast, the poloidal electric field does not develop before reconnection sets in. The charge neutrality is well maintained at the X-point as it ought to be, $(n_i-n_e)/n_i \sim 10^{-3}$. Thus, the poloidal electric field is not triggering the collisionless reconnection process.

The time history of the toroidal current, electric field and the isolated flux are shown in Fig. 9. To compare these results with the magnetized case in Fig. 2, the vertical scales for E_y, J_y and $\Delta\Psi$ are made the same. The growth and saturation of the toroidal current and electric field are quite similar to those observed in the magnetized case. The isolated flux reconnects almost constantly in time in the lower panel if we subtract an oscillatory part due to initial disturbance. Insensitivity to the ambient magnetic field in the $\Delta\Psi \sim t$ regime was reported in the resistive MHD study.[32] Here, the particle simulation gives a more general statement that the reconnection rate is insensitive to the finite ion Larmor radius effect in the time constant flux-reconnection regime. Precise results are found in a separate paper.[34]

IV. DISCUSSIONS

In order to delineate the importance of the electron parallel motion and the resultant transport along the magnetic field line, the hybrid-particle simulation results are first presented. It is well-known in the particle simulation community that the particle method is less susceptible to numerical diffusion than the fully-gridded fluid calculations (e.g., smoothed-particle hydrodynamics). This is because the

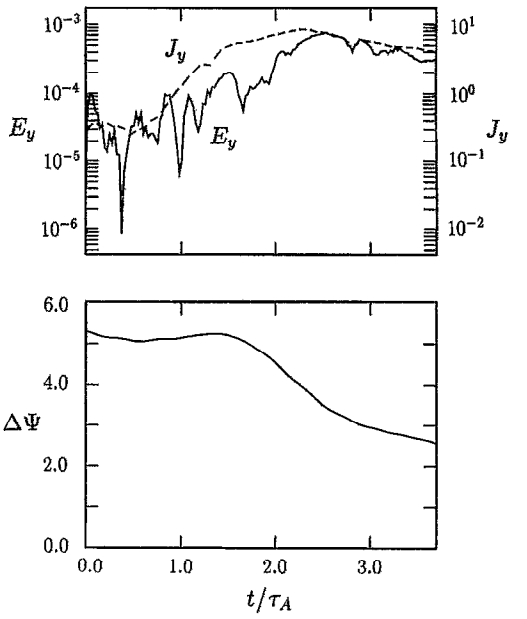

FIG. 9. Time histories of the toroidal electric field (solid) and the toroidal current (dashed) in the upper panel, and the isolated poloidal flux $\Delta\Psi$ in the lower panel for the run with $B_t^{(0)}=0$. Other physical parameters are the same as those of Run A.

source (momentum or current) is carried by the spatially well-defined solid particles in a Lagrangian fashion.

In the hybrid-particle simulation, the electrons are forced to be frozen to the ions in the coordinate space. Namely, the parallel response of the electrons is taken into account through the current term,

$$\frac{dJ_{\parallel}^{(e)}}{dt}=\left(\frac{\omega_{pe}^2}{4\pi}\right)E_{\parallel}, \tag{10}$$

where the parallel direction is determined at every local point. But, their streaming effects on the spatial transport is discarded as in the previous theories[12,15] by imposing on the electrons such that

$$n_e(\mathbf{x})=n_i(\mathbf{x}). \tag{11}$$

Here the ions are treated as particles governed by Eqs. (5) and (6), and their density n_i is calculated by Eq. (9). All the simulation geometry, parameters, and the numerical techniques remain the same as those for Run A in Sec. II.

The time evolutions of the toroidal electric field and current density, and those of the isolated poloidal flux and the separation of the flux bundles for the hybrid-particle simulation are shown in Fig. 10. These results are to be compared with Fig. 2. Obvious differences are that the toroidal current at the X-point is preserved at a higher level in this run compared to Run A, and that magnetic reconnection starts at a later time. More importantly, the poloidal flux reconnects significantly slower than for Run A; the reconnection rate is reduced to $(1/\Delta\Psi^{(0)})(d\Delta\Psi/dt)\sim -0.092\tau_A^{-1}$, which is almost one-third that of Run A. When we take a closer look at the diffusion region in Fig. 11, its shape is even more elongated in the z-direction and its width is narrower but still of the order of the electron skin depth, $L_B \sim c/\omega_{pe}$. Also, the

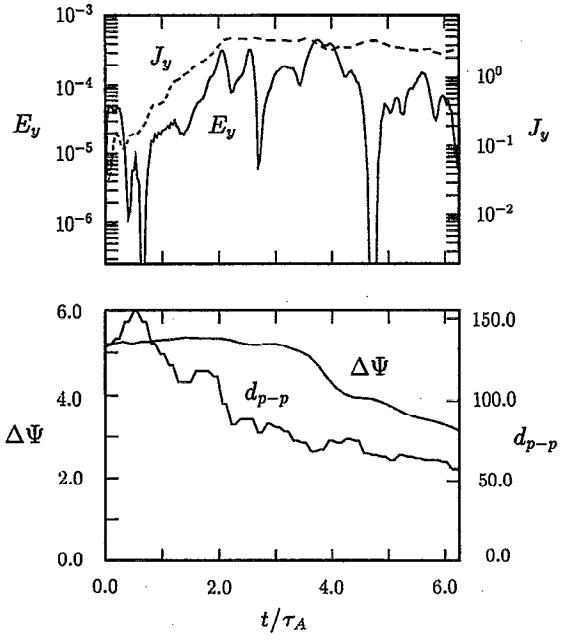

FIG. 10. Results of the hybrid-particle simulation where the parallel electron current is included but their parallel streaming (transport) is ignored by setting $n_e=n_i$. All the other conditions and parameters are the same as those for the simulation in Fig. 2.

dual fan structure with ejected plasma flow which was observed in Fig. 6 becomes less evident. Thus, the excited toroidal current which impedes magnetic reconnection is less efficiently pumped out of the diffusion region under the model where the electron parallel streaming is ignored. These observations are in accordance with the higher current level found in Fig. 10. A complete study of the parallel streaming effects will be presented in the future.

The simulation results described in Secs. II and III will be summarized in the following scenario of collisionless reconnection. The transient process (i) precedes the steady phase (ii) and (iii):

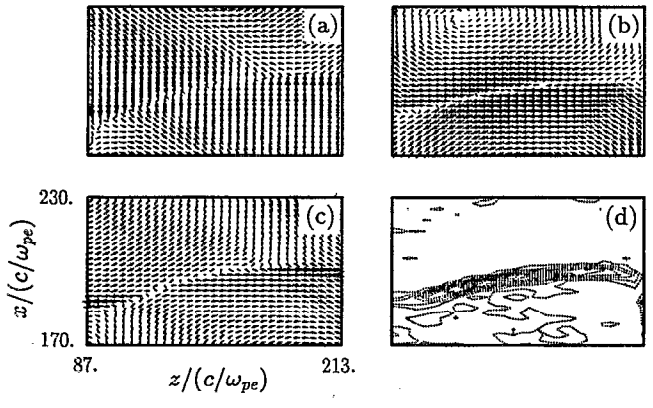

FIG. 11. Enlarged plots of the poloidal quantities for the hybrid-particle simulation. (a), (b) The poloidal electric and magnetic fields, respectively; (c) the poloidal ion current, and (d) the toroidal electron current in the vicinity of the X-point. The maximum norms are (a) $E_p\sim 1.9\times 10^{-2}$, (b) $B_p\sim 0.25$, (c) $J_p^{(i)}\sim 1.1$, and (d) $J_t^{(e)}\sim 8.1$.

(i) In the growth phase, the toroidal electric field E_y is generated by magnetic induction in a broad area extending far beyond the current sheet.
(ii) The steady phase with the finite-amplitude toroidal electric field, $E_y<0$, succeeds the growth phase.
(iii) Magnetic reconnection proceeds in the presence of the toroidal electric field, $\partial \mathbf{B}_p/\partial t=-c\nabla\times(E_y\hat{y})\neq 0$.

The toroidal electric field E_y is purely solenoidal since a charge-separation in the y-direction does not occur in the two-dimensional geometry. A catalytic process in phase (ii) is: the parallel electric field $E_\parallel\cong E_y$ produces the toroidal current J_y in the dissipation region, which gives rise to the proportionality relationship, $E_y\propto J_y$. Outside, by contrast, the electrostatic potential φ, and hence the poloidal electric field E_p, is generated by electron adjustment to shield the parallel electric field,

$$E_\parallel = E_y b_y-\mathbf{b}\cdot\nabla\varphi \cong 0. \tag{12}$$

This poloidal electric field generates, in turn, the sub-Alfvénic $E_p\times B$ plasma outflow. Since the plasma particles carry the current with their motion, this poloidal outflow and parallel streaming result in a constant removal of the toroidal current off the dissipation region. This removal of the toroidal current maintains the steady toroidal electric field in the phase (ii) (cf. Run B). A fast process in ω_{pe}^{-1} time scale is transiently involved which acts to inhibit over-reaction of the plasma and maintain, $\partial E_y/\partial t=c(\nabla\times B_p)_y-4\pi J_y\cong 0$. Actually, $\partial E_y/\partial t$ slightly deviates from zero in such a way to be consistent with the E_y field growth.

The macro-particle simulation has produced the basic results that agree with the previous MHD simulations,[17,19] such as formation of the elongated dissipation region defined by the poloidal magnetic field and the constant flux reconnection rate. On the other hand, the outward plasma flow is not laminar but spreads within the dual fans off the X-point. This feature strongly differs from the rectangular box model of Sweet and Parker, and affects the theoretical reconnection rate based on the concept.[13] Also, there are the following differences from the collisionless MHD studies:

(1) The toroidal electric field is generated in a region much broader than the current sheet (dissipation region), $L_E\gg L_B$.
(2) The width of the current sheet is a few times the electron skin depth, $L_B\sim 3c/\omega_{pe}$, and does not shrink to a smaller scale.
(3) The reconnection rate is insensitive to the Larmor radii of the ions for $\rho_i/L_B\leqslant O(1)$ in the constant-rate reconnection regime.

The above differences are considered to arise from the kinetic approach, Eqs. (1)–(8), where the electron transport along the magnetic field is taken into account. As noted, these equations include the electrostatic field, the inertia and parallel streaming of the electrons as well as gyromotion of the ions. Thus, the static electric field is determined by the self-adjustment of the space charge, and the spatial boundaries of the $E_\parallel<0$ and $J_y<0$ regions are naturally determined instead through violation to the frozen-in condition

via resistivity. A not very spiky current sheet listed in (2) is considered to result from the electron streaming along the magnetic field. This is in line with a "macro" viewpoint that, in order to have steady magnetic reconnection, the current in the dissipation region must saturate in a definite level to limit the repulsive force between the central current sheet and the flux bundles.[33]

It is easily proved that the characteristic time of attraction of the flux bundles is a few Alfvén times if the plasma pressure in the diffusion region is to be ignored. This conclusion will also apply when the toroidal current-carrying plasma (electrons) is efficiently removed out of the region. Let us think of two rods with radius r_0 carrying a current J_0 and mass density ρ_0. The poloidal magnetic field at the rod center which is produced by the other rod is approximated by $B_p = 2J_0/cr$, where r is their separation. Then, the equation of motion for the rod is written,

$$\pi r_0^2 \rho_0 \frac{d^2 r}{dt^2} = -2J_0^2/c^2 r. \tag{13}$$

With a non-dimensional variable $x = r/r_0$, we have

$$\frac{d^2 x}{dt^2} = -\left(\frac{2}{\tau_A^2}\right)\frac{1}{x}, \tag{14}$$

where $\tau_A = r_0/v_A$ with $v_A^2 = B_{p0}^2/4\pi\rho_0 r_0^2$ and $B_{p0} = 2J_0/cr_0$. Multiplying by dx/dt and integrating with the initial condition $(dx/dt)|_0 = 0$, we obtain

$$\left(\frac{1}{\tau_A}\right)\int_0^t dt = \int_0^y \exp(-y^2)\, dy \quad (y = (-\log x)^{1/2}). \tag{15}$$

Then, the coalescence time τ is obtained by setting $y \to \infty$ $(x \to 0)$,

$$\tau \sim \frac{\sqrt{\pi}}{2}\tau_A. \tag{16}$$

This characteristic time is much shorter than that of the $m = 1$ tearing mode.

Measurement of the maximum flow velocity in the poloidal plane gives $v_{out}/v_{in} \sim 3.4$ at $t = 1.6\tau_A$. This is consistent with the observations that the flow is caused by the $E \times B$ drift and that $E_x/E_z \sim 3$. On the other hand, the ratio of the lateral and vertical dimensions of the dual-fan structure in Fig. 6 is obtained to be $l_z/l_x \sim 3$. This reveals that the flux balance is satisfied in the simulation, $l_z v_{in} \sim l_x v_{out}$. It is noted here, however, that the observed inflow and outflow are not aligned with the axes of the rectangular box as invoked in the theory,[13,28,29] but the outflow spreads fully within the fans as shown in the figure. Thus, the effective width of the dissipation region $l_x \sim 30c/\omega_{pe}$ is by one order of magnitude larger than the width $L_B \sim 3c/\omega_{pe}$ as defined by the poloidal magnetic field. Also, the lateral size $l_z \sim 100c/\omega_{pe}$ is a fraction of the *lateral* size of the flux bundle (not $\frac{1}{2}d$). Therefore, the observed reconnection time of a few Alfvén times is close to the reconnection time estimated by the Sweet-Parker model, $\tau_{SP} \sim (l_z/l_x)\tau_A$.

It has been observed in Fig. 2 that the toroidal current and the electric field develop simultaneously at the X-point. As the magnetic field points almost in the toroidal direction there, the net electric field remains unshielded, $E_\parallel \sim E_y$, and can efficiently accelerate the plasma along the magnetic field to produce the large toroidal current. The low-frequency part of the toroidal electric field is treated by Eqs. (1)–(4) neglecting the displacement current $\partial E_y/\partial t$,

$$\nabla^2 E_y \cong \left(\frac{4\pi}{c^2}\right)\frac{\partial J_{Ty}}{\partial t}, \tag{17}$$

with $\mathbf{J}_T$ a divergence-free part of the current $\mathbf{J}$, as the displacement current is a small quantity, $(\partial E_y/c\partial t)/(\nabla \times B_p)_y \sim (L/c\tau)(E_y/B_p) \sim (L/c\tau)^2$, where L is the width of the dissipation region and τ the growth time. If we take $J_y(x,t) = J_0 e^{\gamma t}/\cosh^2(x/L)$ as observed in Sec. II, the electric field may be calculated to be,

$$E_y(x,t) \cong \left(\frac{4\pi\gamma}{c^2}\right) J_0 L^2 e^{\gamma t} \log\cosh(x/L) + F(t). \tag{18}$$

Although this argument is not self-consistent, it at least explains that, for the given current, the toroidal electric field also develops in $e^{\gamma t}$, spatially extending beyond the current sheet.

It has been demonstrated by the implicit and hybrid particle simulations that collisionless reconnection is governed principally by the electrons. A coexistence of the toroidal electric field and current in the dissipation region observed in the present study supports that the equivalent (pseudo-) dissipation in the MHD description is provided by transit acceleration of the "finite mass" electrons.[10] Since the net toroidal electric field remains in the dissipation region, i.e., $E_\parallel \cong E_y$, the toroidal current may be approximated in the first order by

$$J_y^{(e)} = (-e) n \delta v_y^{(e)} \cong (ne^2/m_e) E_y \tau_{tr}. \tag{19}$$

Here, τ_{tr} is an electron transit time through the dissipation region which is a few Alfvén times in the coalescence process. The transit time is determined passively by the poloidal $E_p \times B$ drift speed and the streaming along the magnetic field. The proportionality relationship between J_y and E_y in Eq. (19) agrees well with the observation in Fig. 2. Equation (19) is cast in the form of the collisionless Ohm's law,

$$E_y \cong \eta_{eq} J_y, \tag{20}$$

where $\eta_{eq} = 4\pi/\omega_{pe}^2 \tau_{tr}$ is the equivalent resistivity (no real dissipation). Substitution of Eq. (20) into the Ampère's law yields the toroidal electric field, $E_y \cong (c\tau_{tr}/L_B) B_p/(1 + \omega_{pe}^2 \tau_{tr}^2)$, where $L_B = (\partial \log B_p/\partial x)^{-1}$. With the Faraday's law, we obtain the width of the dissipation region,

$$L_B^{(th)} \cong c/\omega_{pe}. \tag{21}$$

The same result was derived by the MHD equations and the Ohm's law with the electron inertia current.[13] It is again noted that this value gives the width of the current sheet or the dissipation region defined by the poloidal magnetic field, as seen in Fig. 6, which is smaller than that of the effective width defined by the plasma outflow.

One of the most sophisticated issues of collisionless reconnection is removing the singularity at the X-point. The fluid inertia term behaves like $E_\parallel \sim \partial J_\parallel/\partial t + (\mathbf{v}\cdot\nabla) J_\parallel \to 0$ at

the X-point. Thus, a small but finite resistivity $\eta J_\parallel \neq 0$ is required in the MHD theories[11–16] to break and reconnect the magnetic field. In the particle simulation, only a few particles pass right through this infinitesimally small X-point, and they may be easily scattered and escape this singularity either along the magnetic field or poloidally by random (non-symmetric) $\delta\mathbf{E}_\perp \times \mathbf{B}$ motion due to fluctuating $\delta\mathbf{E}_\perp$ field or micro-instabilities. Once off the X-point, the $E_p \times B$ and ∇B drifts carry them steadily away, which means removal of the toroidal current. The current saturation at the X-point will maintain the finite electric field, $E_y < 0$, and result in steady magnetic reconnection.

V. SUMMARY AND CONCLUDING REMARKS

In this paper, the basic process of collisionless magnetic reconnection was investigated using the electromagnetic, implicit particle simulation method (the "HIDEN" code). As the two magnetic flux bundles approached, the toroidal electric field that directly relates to magnetic reconnection was induced solenoidally in the area much broader than the current sheet. An elongated current sheet was also formed whose width is a few electron skin depths. A remarkable observation was that the plasma outflow was not confined in a narrow channel defined by the poloidal magnetic field, but it spread within the open fans originating at the X-point. The effective width of the dissipation region is thus by one order of magnitude larger than that defined by the current sheet (i.e., the poloidal magnetic field). This feature substantially differs from the rectangular box model of Sweet and Parker. Also, the current sheet did not collapse to a smaller scale but became broad after reconnection, owing to parallel streaming of the electrons.

The poloidal outflow of the plasma was observed to be sub-Alfvénic at the exits of the dissipation region. The poloidal electric field resulting from electrostatic shielding of the inductive electric field acted as a catalyst of generating the $E_p \times B$ plasma flow in the magnetized case. Significant electron acceleration in the toroidal direction, $v_\parallel \sim 5 v_A$, was observed at the X-point. The observed bi-modal velocity distribution function for the electron parallel motion was a consequence of acceleration, and was not a direct thermalization. This is consistent with that the whole process occurs in a collisionless plasma. Competition of transit electron acceleration due to the non-shielded toroidal electric field and their removal by the poloidal outflow was considered to control the toroidal current and, hence, the reconnection rate.

The implicit particle simulation showed primary dominance of the electron dynamics in the collisionless reconnection process. This observation was justified by the hybrid-particle simulation where the electron parallel current was incorporated through $dJ_\parallel^{(e)}/dt = (\omega_{pe}^2/4\pi)E_\parallel$ but the electrons were spatially frozen to the ions as $n_e = n_i$. Without the parallel transport (streaming), the reconnection rate was significantly reduced. The observed toroidal current and electric field supported that the equivalent resistivity in the MHD theory is provided by the transit acceleration of the finite-mass electrons through the dissipation region. This yielded the collisionless Ohm's law $E_t \sim \eta_{eq} J_t$ with η_{eq} the inertia resistivity, which gave the width of the dissipation region (defined by the poloidal magnetic field) to be an electron skin depth.

For the rather flat initial magnetic profile corresponding to the square currents, the magnetic flux reconnected constantly in time in the steady phase. In the other series of runs with Fadeev's equilibrium, the reconnection rate increased with time for the highly-peaked initial magnetic profile. However, the reconnection rate was insensitive to the finite Larmor radii of the ions in the constant-rate flux reconnection regime even for $\rho_i > L_B$.

Finally, a complete study of parallel streaming effects and an investigation of the ion kinetic effects in the nonlinear reconnection regime are currently undertaken. A three-dimensional study of collisionless magnetic reconnection is also an attractive and challenging problem. Although the present two-dimensional simulations include most essential features of the collisionless reconnection, the addition of the third dimension may modify the process. Namely, a coupling of the toroidal current to the current-driven instabilities may give rise to additional dissipation and limit the toroidal current. Further, global redistribution of the electrons along the magnetic field may affect the toroidal electric field and the reconnection rate. These issues await future studies by particle simulations.

ACKNOWLEDGMENTS

The author gratefully acknowledges valuable discussions with Dr. J. U. Brackbill and Dr. J. Todoroki on the ill-conditioned matrix inversion which occasionally appears in the solution of the coupled equations of the HIDEN implicit particle code. He thanks Dr. A. Bhattacharjee, Dr. A. Aydemir, Dr. M. Yamada and Dr. J. W. Van Dam for encouraging discussions.

[1] J. W. Dungey, Philos. Mag. **44**, 725 (1953).
[2] M. N. Rosenbluth, R. Y. Dagazian, and P. H. Rutherford, Phys. Fluids **16**, 1894 (1973).
[3] B. B. Kadomtsev, Fiz. Plasmy **1**, 710 (1975) [Sov. J. Plasma Phys. **1**, 389 (1975)].
[4] W. Park, D. A. Monticello, and R. B. White, Phys. Fluids **27**, 137 (1984).
[5] D. Biskamp, Phys. Fluids **29**, 1520 (1986).
[6] R. C. Davidson and N. T. Gladd, Phys. Fluids **18**, 1327 (1975).
[7] J. D. Huba, N. T. Gladd, and K. Papadopoulos, J. Geophys. Res. **83**, 5217 (1978).
[8] W. Horton and T. Tajima, J. Geophys. Res. **96**, 15811 (1991).
[9] B. Coppi, Phys. Fluids **8**, 2273 (1965).
[10] T. W. Speicer, Planet. Space Sci. **18**, 613 (1970).
[11] J. F. Drake, Phys. Fluids **21**, 1777 (1978).
[12] J. F. Drake and R. G. Kleva, Phys. Rev. Lett. **66**, 1458 (1991).
[13] J. A. Wesson, Nucl. Fusion **30**, 2545 (1990).
[14] A. Y. Aydemir, Phys. Fluids B **2**, 2135 (1990).
[15] M. Ottaviani and F. Porcelli, Phys. Rev. Lett. **71**, 3802 (1993).
[16] L. Zakharov, B. Rogers, and S. Migliuolo, Phys. Fluids B **5**, 2498 (1993).
[17] D. Biskamp and H. Welter, Phys. Rev. Lett. **44**, 1069 (1980).
[18] F. L. Waelbroeck, Phys. Fluids B **1**, 2372 (1989).
[19] X. Wang and A. Bhattacharjee, Phys. Fluids B **4**, 1795 (1992).
[20] T. Tajima, F. Brunel, and J. Sakai, Astrophys. J. **258**, L45 (1982).
[21] D. W. Hewett, G. E. Francis, and L. E. Max, Phys. Rev. Lett. **61**, 893 (1988).
[22] M. Tanaka, EOS Trans. (Am. Geophys. Union) **75**, 263 (1994).

[23]M. Tanaka, J. Comput. Phys. **107**, 124 (1993); **79**, 209 (1988).
[24]B. Coppi, S. Migliuolo, F. Pegoraro, and F. Porcelli, Phys. Fluids B **2**, 927 (1990).
[25]E. R. Priest, *Solar Magnetohydrodynamics* (Reidel, Dordrecht, 1982).
[26]H. X. Vu and J. U. Brackbill, Comput. Phys. Comm. **69**, 253 (1992).
[27]M. Yamada, Y. Ono, A. Hayakawa, M. Katsurai, and F. W. Perkins, Phys. Rev. Lett. **65**, 721 (1990).
[28]P. A. Sweet, Nuovo Cimento **8**, 188 (1958).
[29]E. N. Parker, Astrophys. J. Suppl. **77**, 177 (1963).
[30]V. M. Fadeev, I. F. Kvartshkhava, and N. N. Kamarov, Nucl. Fusion **5**, 202 (1965).
[31]M. Tanaka, *Theory of Fusion Plasmas*, edited by F. Troyon and E. Sindoni (Societa Italiana di Fisica, Bologna, 1994), pp. 233–246.
[32]A. Bhattacharjee, F. Brunel, and T. Tajima, Phys. Fluids **26**, 3332 (1983).
[33]M. Yamada (private communication, 1994).
[34]M. Tanaka, Comput. Phys. Commun. **87**, 117 (1995).